Fast long-distance transport of cold cesium atoms

Till Klostermann,[1,2,3] Cesar R. Cabrera,[1,2,3] Hendrik von Raven,[1,2,3] Julian F. Wienand,[1,2,3] Christian Schweizer,[1,2] Immanuel Bloch,[1,2,3] and Monika Aidelsburger[1,2]

[1]*Fakultät für Physik, Ludwig-Maximilians-Universität, Schellingstrasse 4, D-80799 München, Germany*
[2]*Munich Center for Quantum Science and Technology, Schellingstrasse 4, D-80799 München, Germany*
[3]*Max-Planck-Institut für Quantenoptik, Hans-Kopfermann-Strasse 1, D-85748 Garching, Germany*

(Received 21 September 2021; revised 27 February 2022; accepted 5 April 2022; published 26 April 2022)

Transporting cold atoms between distant sections of a vacuum system is a central ingredient in many quantum simulation experiments, in particular in setups, where large optical access and precise control over magnetic fields is needed. In this work, we demonstrate optical transport of cold cesium atoms over a total transfer distance of about 43 cm in less than 30 ms. The high speed is facilitated by a moving lattice, which is generated via the interference of a Bessel and a Gaussian laser beam. We transport about 3×10^6 atoms at a temperature of a few microkelvins with a transport efficiency of about 75%. We provide a detailed study of the transport efficiency for different accelerations and lattice depths and find that the transport efficiency is mainly limited by a fast initial loss most likely due to the sudden onset of the acceleration and the potential depth along the direction of gravity. To highlight the suitability of the optical-transport setup for quantum simulation experiments, we demonstrate the generation of a pure Bose-Einstein condensate with about 2×10^4 atoms. We find a robust final atom number within 2% over a duration of 2.5 h with a standard deviation of <5% between individual experimental realizations.

DOI: 10.1103/PhysRevA.105.043319

I. INTRODUCTION

Ultracold atoms in optical lattices are powerful platforms for quantum simulation of complex quantum many-body systems [1], most notably in the context of condensed-matter physics [2–4]. Recent advances further opened up promising new directions [5–9] to study phenomena related to quantum gravity [10–12], quantum electrodynamics, and high-energy physics [13,14]. The precise parameter control and natural scalability of neutral-atom devices enable analog quantum simulation with hundreds of atoms, which significantly challenges the limits of state-of-the-art numerical methods [15–18]. Moreover, neutral atoms offer a broad range of applications in quantum metrology and sensing [19] and digital quantum computing [20].

For high-fidelity operation large optical access [21], a clean electromagnetic environment, and excellent vacuum conditions are indispensable. These are often achieved by separating the main experimental apparatus into two distinct sections: one chamber for preparation and precooling of the cold atomic cloud and a second science chamber where the actual measurements are performed (Fig. 1). Such a two-chamber design naturally requires transporting the atoms between the two separate vacuum sections. However, this usually comes at the expense of increased experimental complexity and longer cycle times. On the other hand, reaching faster cycle times [22–29] and developing compact and robust experimental setups [30] are essential for the development of the next generation of quantum devices [31–34].

There are various different transport schemes that have been developed which make use of magnetic [35–37], optical [38–46], or hybrid [40,41] traps. Magnetic transport typically relies on the translation of the trap minimum either by dynamically controlling the current in overlapping pairs of coils [35] or by mechanically moving a single pair of coils [36,37]. While magnetic transport has been demonstrated reliably for large distances, it requires complex mechanical engineering, typically limits the optical access, and is applicable to only magnetically trappable atoms. Optical transport, on the other hand, can be implemented for any atomic species, although typically at reduced trap depths. The most straightforward implementation is based on a mechanically movable lens that generates a tightly focused optical dipole trap with variable focus position [43,47]. Since moving mechanical parts introduce vibrations, novel schemes based on focus-tunable lenses [42,45] have been developed. However, the total transport duration for all schemes mentioned above is fundamentally limited either by small longitudinal trapping frequencies or by the finite velocities of the mechanical stages, which results in transport times on the order of a second for typical transport distances. This motivates the use of running-wave optical lattices, where the motion is controlled via the frequency detuning of two counterpropagating laser beams. This configuration offers large longitudinal trapping frequencies, and no moving components are needed [38,39,44].

Here we report fast optical transport of ^{133}Cs atoms over an unprecedented distance of 43 cm (86 cm round trip) in < 30 ms (60 ms) using a far-detuned running-wave optical lattice, for which we reach final velocities of up to 26.6 m/s. Due to the large mass of cesium, large optical gradients are required during transport. Therefore, the running-wave lattice is generated by the interference of a Bessel and a Gaussian laser beam (Fig. 1), similar to what was used in Ref. [39].

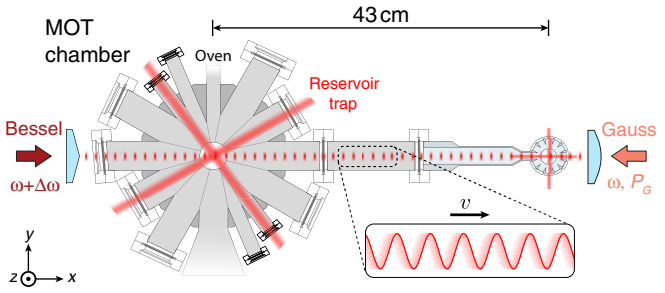

FIG. 1. Experimental setup. Vacuum system with a two-chamber design: precooling in a magneto-optical trap (MOT) is performed in the first chamber, and the final evaporation to Bose-Einstein condensation takes place in the glass cell. The distance between the two chambers is 43 cm. The atom source (oven) is connected to the top port. The crossed-dipole beams, which form the reservoir trap in the MOT chamber and the dipole trap (X, Y) for evaporation in the glass cell, are shown in red. The transport lattice (red dots) is formed by the interference of two counterpropagating laser beams: a Bessel beam (dark red arrow) with frequency $\omega + \Delta\omega$ (left), which is generated by sending a laser beam of 35 W onto an axicon, and a Gaussian laser beam (light red arrow) with frequency ω and variable power P_G, which is focused between the two chambers by a lens. The detuning $\Delta\omega = 2\pi\,\Delta f$ results in a running-wave lattice that moves with velocity v.

We observe a one-way transport efficiency of ∼75% and demonstrate the robustness of the scheme by generating a Bose-Einstein condensate (BEC). The mean atom number is stable within 2% over the course of 2.5 h, making this scheme suitable for state-of-the-art quantum simulation experiments using heavy atoms such as ^{133}Cs.

II. EXPERIMENTAL SETUP

Our experimental apparatus consists of two main vacuum chambers separated by 43 cm (Fig. 1). The magneto-optical trap (MOT) chamber is a steel chamber, where all precooling steps are performed: MOT, optical molasses, and degenerate Raman sideband cooling (see Sec. A 5 and Fig. 13 therein). The science chamber is a glass cell with large optical access in order to support single-atom single-site manipulation and readout [48–56] using a high-numerical-aperture (NA) objective that is placed outside the vacuum chamber. Moreover, it has 11 side ports, which can be used for optical lattices and additional dipole potentials.

A. Optical transport setup

The large mass m of ^{133}Cs requires large optical gradients to hold the atoms against gravity. The diffraction of Gaussian beams makes this challenging to achieve because large laser powers are required for a sufficiently steep trap over the full transport distance. To circumvent this issue we employ a Bessel beam that is generated using an axicon [39]. It has a diffractionless range $x_B = w_0 \tan(\alpha/2)/(n-1)$, which depends on the apex angle α of the axicon, the waist w_0 of the incoming Gaussian laser beam, and the axicon's refractive index n [Fig. 2(a)], as described, e.g., in Refs [39,57]. Within the range x_B the radius of the central spot of the beam profile

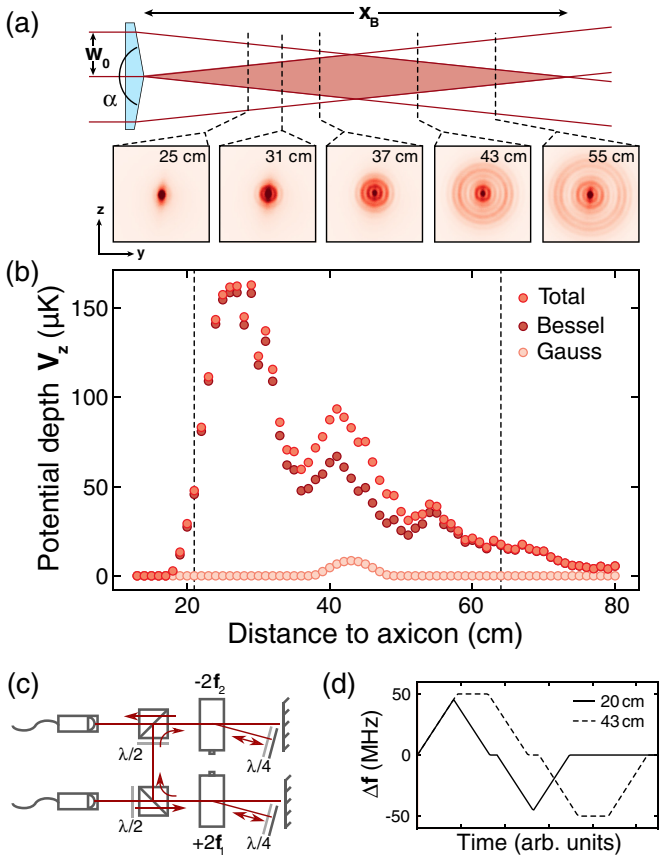

FIG. 2. Transport setup. (a) Realization of the Bessel beam with an axicon with apex angle α and an incoming Gaussian laser beam with waist w_0. Two-dimensional images show measured beam profiles at different distances from the axicon. The diffractionless range is given by x_B. (b) Vertical trap depth V_z of the Gaussian transport beam (light red dots), the Bessel beam (dark red dots) and the combined trap (medium red dots) versus distance from the axicon taking gravity into account. The depth is computed using the measured beam profiles of the Bessel beam (power of incoming laser beam: 35 W) and the focal position of the Gaussian beam at $P_G^{\mathrm{typ}} = 6.5$ W. The dashed vertical lines indicate the start and end point of the transport. (c) Schematic setup used to control the frequency offset Δf between the two transport beams. A small amount of light is split off from the laser generating the Gaussian transport beam. Two DPAOM setups with dynamically tunable rf frequencies $f_1(t)$ and $f_2(t)$ are used to introduce frequency detunings up to 50 MHz each. The setup is fiber coupled and used to seed a second amplifier, which generates light for the Bessel-shaped transport beam. (d) Simplified schematic illustrating the frequency ramps for the round-trip transport for two different transport distances. Positive Δf corresponds to transport in the direction of the glass cell.

remains approximately constant [Fig. 2(a); see also Fig. 7 in Sec. A 1]. For an ideal axicon, the $1/e^2$ waist of the central peak is $w_B \simeq 1.8\cos(\alpha/2)/k(n-1)$, and its intensity follows a Gaussian shape; $k = 2\pi/\lambda$ is the wave vector, and λ is the wavelength of the laser beam. Imperfections at the tip of the axicon result in additional oscillations of the intensity along the transport axis [Fig. 2(b); see also Fig. 8 in Appendix A]. In our case we use an axicon with an apex angle $\alpha = 179°$ and a laser beam with $\lambda = 1064$ nm and $w_0 = 2.5$ mm. This

results in a central spot with waist $w_B = 80\,\mu$m and sufficient peak intensity over the full transport distance of 43 cm [see Fig. 7(b) in Sec. A 1]. The Bessel beam acts as a waveguide that holds the atoms against gravity, and the interference with the Gaussian laser beam forms the transport lattice. For the latter we employ a rather large waist of $600\,\mu$m and find that a moderate power of $P_G^{\text{typ}} = 6.5$ W is enough for optimal transport efficiencies. The focus position of the beam was optimized by maximizing the transport efficiency. The optimum was found about 21 cm away from the center of the glass cell.

B. Control of the detuning

The two counterpropagating laser beams form a one-dimensional (1D) optical lattice $V(x) \propto \sqrt{P_G}\sin(2kx + 2\pi\Delta f\, t/2)$. Here Δf is the frequency difference between the two beams, which results in a moving lattice with velocity $v = \lambda\Delta f/2$. For fast and accurate transport, the detuning needs to be accurately controlled with a large bandwidth. This is achieved using direct digital synthesis (DDS) and acousto-optic modulators (AOMs) in double-pass configuration (DPAOMs), as illustrated in Fig. 2(c).

In order to avoid a frequency-offset lock, we use two separate fiber amplifiers at 1064 nm to generate the transport laser beams. We split off light from one of them and use it to seed the second amplifier. In between, we implement a frequency-shifting setup that consists of two DPAOMs with dynamically tunable frequencies f_1 and f_2. This enables broadband tuning, where each DPAOM can introduce a detuning up to $\Delta f = 50$ MHz, which corresponds to a lattice velocity $v \approx 26.6$ m/s. In combination with the large trap frequencies in the lattice along the transport direction, accelerations up to several thousand m/s^2 can be achieved.

III. REALIZATION OF LARGE-DISTANCE OPTICAL TRANSPORT

A. Loading of the transport lattice

To facilitate loading of low-temperature atoms into the transport lattice, we transfer the dilute, precooled cloud into a large volume reservoir trap and add the Bessel beam at low intensity to act as a tightly focused optical dimple [58]. The thermalization between the atoms in the reservoir and the dimple (Bessel) enables high densities at low temperatures in the transport lattice.

The sequence starts by collecting Zeeman-slowed ^{133}Cs atoms in a MOT within 3 s, which are further cooled in an optical molasses using standard techniques (see Sec. A 5). To further cool and spin polarize the atoms we use degenerate Raman sideband cooling in a near-detuned optical lattice [59], which results in a cold atomic cloud of about 2×10^7 atoms in the absolute ground state $|F = 3, m_F = 3\rangle$ at $< 1\,\mu$K with a peak density of $n_0 = 3 \times 10^{10}$ atoms/cm^3. When loading the atoms adiabatically into a crossed-beam dipole trap, the phase-space density (PSD) $\phi = n_0\lambda_{dB}^3$ is conserved; here $\lambda_{dB} = h/\sqrt{2\pi m k_B T}$ denotes the thermal de Broglie wavelength, h is Planck's constant, k_B is Boltzmann's constant, and T is the temperature of the atoms. To limit the temperature increase, the Raman-cooled cloud is transferred into a shallow, large-volume crossed-dipole trap, which is formed by a single laser beam passing through the MOT chamber in a bow-tie configuration at a wavelength of 1064 nm with a circular waist of 0.5 mm and a maximum power of 15 and 10 W in the first and second pass, respectively. The power difference between the beams is due to transmission losses from the vacuum-chamber view ports and nonoptimal angle of incidence and polarization of some of the mirrors reflecting the second dipole trap arm. In addition, we apply a magnetic field gradient of 31.3 G/cm to hold the atoms against gravity. For efficient thermalization during loading, we further apply a magnetic offset field of 120 G to increase the s-wave scattering length to $a \approx 1500a_0$ [60]; here a_0 denotes the Bohr radius. After a hold time of 250 ms we obtain 6×10^6 atoms at $3\,\mu$K in the crossed-dipole trap.

During the next 400 ms we ramp up the power of the Bessel beam to 20 W and let the atoms rethermalize. To load the atoms into the 1D transport lattice, we then redirect all power from the reservoir beams to the Bessel beam within 500 ms and simultaneously ramp up the Gaussian beam to 6.5 W to avoid spreading of the cloud along the Bessel beam. The magnetic offset field is changed to 23 G ($300a_0$) to reduce three-body losses. After the reservoir has been fully removed, we end with about 4×10^6 atoms at $10\,\mu$K in the static transport lattice. We attribute the large increase in temperature compared to the reservoir trap to compression in the 1D lattice.

B. Transport efficiency

Optical transport in the running-wave lattice is realized by linearly increasing the detuning Δf between the two counterpropagating lattice beams, which results in a constant acceleration a. Before the atoms reach the final position in the glass cell, we apply a linear deceleration ramp, where the detuning is decreased to zero at the same rate as during the acceleration. For typical parameters ($a_{\text{typ}} = 2.9$ km/s^2, $P_G^{\text{typ}} = 6.5$ W), we obtain a final transport velocity of 26.6 m/s, and the transport duration for the full distance to the glass cell is 25.5 ms. After transport, we find a total of 3×10^6 atoms in the glass cell at a temperature of $5\,\mu$K. This corresponds to a transport efficiency of ∼75%. We attribute the reduced temperature in the glass cell to evaporation during transport. The magnetic offset field in the glass cell is set to 28.2 G ($480a_0$) during transport. Note that there are no additional bias fields along the transport axis. Nonetheless, we do not observe any spin depolarization.

To investigate the transport efficiency as a function of the transport distance, we perform round-trip measurements, where the atoms are transported back into the MOT chamber [Figs. 3(a) and 3(b)]. We scan the final position between the MOT chamber and the glass cell by changing the time between the acceleration and deceleration ramps [Fig. 2(d)]. At the beginning of the transport ($100\,\mu$s), we observe a sharp decrease in the atom number. Varying the acceleration [Fig. 3(a)] up to 4.0 km/s^2 does not lead to a significant further change. Reducing the lattice depth, on the other hand [Fig. 3(b)], results in a significant increase in the atom loss. We attribute this initial loss to the sudden onset of the acceleration, which limits the number of atoms that are transported. This could be improved in future experiments by implementing

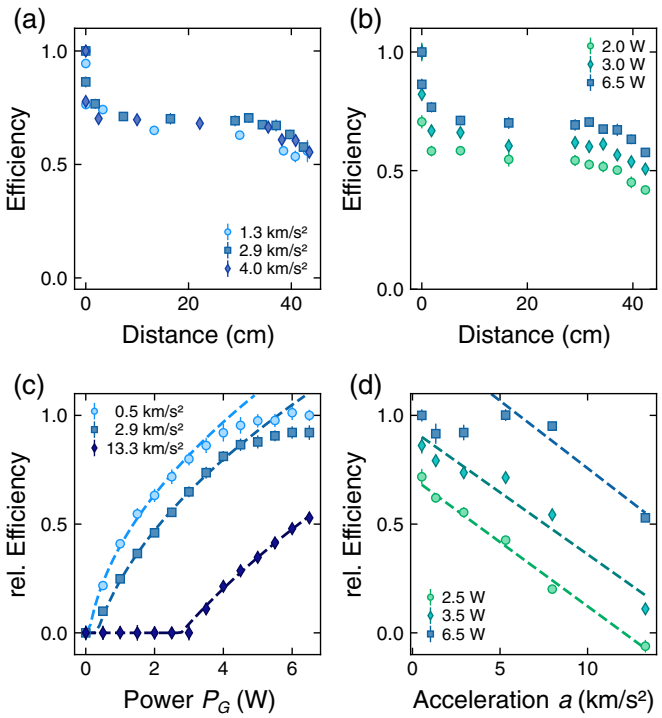

FIG. 3. Transport efficiency. Efficiency of round-trip transport versus transport distance: (a) different accelerations a for $P_G^{\mathrm{typ}} = 6.5$ W and (b) different lattice depths for $a_{\mathrm{typ}} = 2.9\,\mathrm{km/s^2}$. The lattice depth is varied by changing the power of the Gaussian transport beam P_G. Relative efficiency of one-way transport to the glass cell versus (c) power P_G for three different accelerations a and (d) acceleration a for three different Gaussian powers P_G. Relative efficiency is defined as the ratio of the transported atom number to the transported atom number at low acceleration and large Gaussian power (Sec. A 3 c). The dashed lines are guides to the eye. In (c) the dashed line shows a scaling with $\sqrt{P_G}$; in (d) the scaling is linear with acceleration a. Error bars show the standard error of the mean, extracted from five repetitions in (a)–(d).

nonlinear frequency ramps [39,47,61,62]. In addition, we observe a reduction in the transport efficiency for the longest distances, which becomes more pronounced for larger accelerations and weaker lattice depths. This is most likely caused by the smaller lattice depth (see Fig. 9) and the reduced vertical trap depth [Fig. 2(b)] near the center of the glass cell. For typical parameters (a_{typ}, P_G^{typ}) we measure round-trip efficiencies for the full distance (86 cm) to the science cell of >50%, which is consistent with a one-way transport efficiency of 75%. Residual deviations are most likely explained by systematic uncertainties in the atom-number calibration.

To gain more insight about the dependence of the transport efficiency on the depth of the lattice [Fig. 3(c)] and the acceleration [Fig. 3(d)], we evaluate the one-way transfer efficiency in the glass cell. We observe a scaling with $\sqrt{P_G}$ for low efficiencies, which suggests that the transport efficiency depends linearly on the depth of the lattice potential. Moreover, with increasing acceleration it falls off approximately linearly [Fig. 3(d)]. Again, this suggests a linear dependence on the lattice depth, if we consider the effective depth of the potential in the presence of a tilt that is generated by the acceleration. The saturation of the transport efficiency for high values of P_G and low accelerations a indicates that these parameters are not the dominating limitations of the observed transport efficiency of 75%. The main limitations are most likely the fast initial loss due to the sudden onset of the acceleration and atoms that are lost during transport due to gravity. Note that changing P_G predominantly changes the lattice depth and has only a minor impact on the trap depth in the vertical direction that holds the atoms against gravity.

IV. GENERATION OF A BOSE-EINSTEIN CONDENSATE

A. Dipole trap and optical evaporation

After the atoms are transported into the glass cell they are levitated with a magnetic field gradient and collected in a crossed-optical-dipole trap at 1064 nm. The beam along y is elliptical with a waist of $650 \times 80\,\mu\mathrm{m}^2$ in the xz plane and a maximum power of 5.7 W, matched to the atomic cloud shape after transport. The one along x is circular with a 50-μm waist and a maximum power of 350 mW (Fig. 1). We load the dipole trap by first ramping up the dipole trap along y to full power and the Gaussian transport beam to zero in 350 ms. After the transport lattice is fully removed, we ramp up the dipole beam along x in 100 ms to full power. We then reduce the offset field to 27 G ($440a_0$) in 200 ms. The end of the offset field ramp defines $t = 0$ in Figs. 4(a)–4(c). Next, we perform a short optical evaporation, where the Bessel transport beam is turned off (500 ms) and at the same time the power of the dipole beam along y is reduced to 2 W. At this point [blue dashed line in Fig. 4(c)] we have 9×10^5 atoms at 2 μK and a PSD of $\phi = 3 \times 10^{-3}$. The corresponding *in situ* peak density is $n_0 = N\bar{\omega}^3(m\lambda_{dB}/h)^3 = 6 \times 10^{11}/\mathrm{cm}^3$ [63], where the geometric-mean trap frequency is calibrated to be $\bar{\omega} = 2\pi \times 40$ Hz.

B. Gradient evaporation

To reach degeneracy we use the technique of forced evaporative cooling in a way similar to what was done in Ref. [63]. We reduce the levitation gradient linearly in two successive steps to tilt the dipole potential. This allows us to keep large trapping frequencies and hence large thermalization rates during evaporation. In Fig. 4(c) we show the PSD during evaporation, which was evaluated using the calibrated atom numbers [Fig. 4(a)], trap frequencies, and temperatures [Fig. 4(b)]. We optimize the parameters of the evaporation ramps experimentally by maximizing the evaporation efficiency $\eta = -\ln(\phi_f/\phi_i)/\ln(N_f/N_i)$ after each step; here the indices i and f denote the parameters at the beginning and end of the evaporation step. We find the following optimized sequence (see Fig. 13 in Sec. A 5): During the first step, the gradient is reduced linearly to 11.5 G/cm in 500 ms. The second step is a hybrid evaporation scheme, where the gradient is switched off within 5 s, and the power of the dipole beam along x is reduced to 160 mW in 2 s. The magnetic offset field is lowered to 23 G ($a \approx 300a_0$), which was found to be the optimal ratio of elastic collisions and three-body losses [58,60]. The evaporation sequence described above typically results in a BEC with 2.2×10^4 atoms without any discernible thermal fraction and evaporation efficiencies of $\eta = 1.3$ for

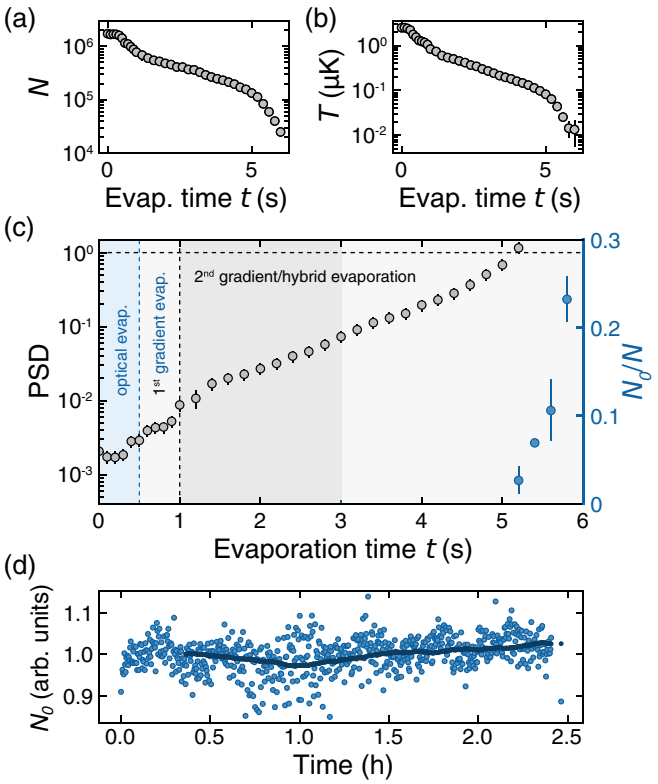

FIG. 4. Evaporation to BEC. Evolution of (a) atom number N, (b) temperature T, and (c) PSD (gray dots) and BEC fraction N_0/N (blue dots) during evaporation. The shaded regions indicate the evaporation steps: optical evaporation (blue) and gradient evaporation (gray). The additional optical evaporation during the second gradient evaporation is shown in dark gray. The blue dashed line shows the end of the optical evaporation, and the black one shows the end of the first gradient evaporation. Error bars indicate 1σ standard deviation for three repetitions. (d) Fluctuations of the normalized BEC atom number N_0 over a period of ∼2.5 h (light blue points). The 1σ standard deviation is <5%. Dark blue points show the mean values of the individual data points, averaged over 20-min intervals. The 1σ standard deviation is <2%.

the first step and $\eta = 2.5$ for the second. The final values for the BEC fraction at the end of the evaporation sequence are not shown in Fig. 4(c) since the small thermal fraction cannot be reliably extracted from the data anymore.

The total cycle time is 11.5 s, comparable to other experiments without transport [63–65]. We test that the duration of the evaporation ramps can be reduced further at the expense of reduced total atom numbers. With a total cycle time of 7.5 s we obtain pure BECs with 1×10^4 atoms. Finally, to demonstrate the stability of our transport and its suitability for quantum simulation experiments, we measure the final atom number in the BEC over 2.5 h and find that it fluctuates by <5% and the mean value (averaged over 20 min) drifts by <2% [Fig. 4(d)]. This is comparable to the atom-number fluctuations before transport (see Sec. A 4), indicating that it does not induce additional instabilities.

V. CONCLUSION

In conclusion, we have demonstrated stable optical transport of heavy ^{133}Cs atoms over a large distance of 43 cm in less than 30 ms with good efficiency and without observable heating. The transport efficiency seems to be predominately limited by the temperature of the atoms and potential depth along the vertical direction. Larger accelerations may further require the implementation of smoother frequency ramps. The fast transport setup demonstrated here enables short cycle times, which will be beneficial for improved statistics in future experiments. The cycle time could be reduced further by implementing additional all-optical cooling techniques [26–29] to reduce the loading and evaporation times in the dipole traps. Our design further facilitates large optical access, enabling the installation of high-NA objectives for single-atom single-site-resolved imaging and manipulation of cold ^{133}Cs atoms in optical lattices [48–56].

The data that support the plots within this paper and other findings of this study are available from the corresponding author upon request. The code that supports the plots within this paper is available from the corresponding author upon request.

ACKNOWLEDGMENTS

We acknowledge insightful discussions with C. Chin and his team, E. Haller, and H.-C. Nägerl. The authors acknowledge A. Reetz for help in characterizing the Bessel-beam profile and performing calculations for the design of the setup and J. Chen for help in setting up the frequency-detuning setup and characterization of the pointing stability of the Bessel beam. This work was supported by the Deutsche Forschungsgemeinschaft (DFG, German Research Foundation) under Project No. 277974659 via Research Unit FOR 2414. The work was further funded by the Deutsche Forschungsgemeinschaft (DFG, German Research Foundation) under Project No. 452143229 and under Germany's Excellence Strategy, EXC-2111390814868. T.K. was supported by the Bavarian excellence network ENB via the International Ph.D. Programme of Excellence Exploring Quantum Matter (ExQM). C.R.C. acknowledges support from the ICFO-MPQ Cellex postdoctoral fellowship and from the European Union (Marie Skłodowska-Curie Grant No. 897142). H.v.R. acknowledges support from the Hector Fellow Academy. J.F.W. acknowledges support from the German Academic Scholarship Foundation. C.S. has received funding from the European Union's Framework Programme for Research and Innovation Horizon 2020 (2014-2020) under Marie Skłodowska-Curie Grant Agreement No. 754388 (LMUResearchFellows) and from LMUexcellent, funded by the Federal Ministry of Education and Research (BMBF) and the Free State of Bavaria under the Excellence Strategy of the German Federal Government and the Länder.

APPENDIX

1. Characterization of optical transport setup

Bessel beam. To compute the vertical trap depth V_z along the transport direction in Fig. 2(a), we measure the Bessel beam profile at different positions behind the axicon. To ensure that the camera is not saturated we work at low power. The axicon is made from fused silica ($n = 1.45$ at 1064 nm [66]), and the incident beam has low intensity even at

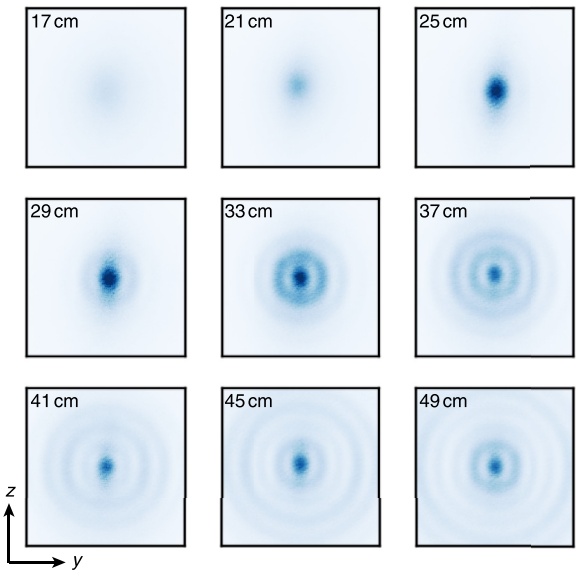

FIG. 5. Bessel beam profile along x, the transport direction, for the parameters $\alpha = 179^\circ$, $w_0 = 2.5$ mm, and $\lambda = 1064$ nm. The distance from the axicon is indicated in the top left corner of each image.

35-W power due to the large waist ($w_0 = 2.5$ mm), so thermal lensing in the axicon is assumed to be negligible.

During the first few centimeters behind the axicon the profile of the beam is still Gaussian. About 25 cm behind the axicon, the first diffraction ring appears, and the profile becomes more Bessel-like (Fig. 5). In order to extract a peak intensity for computing the dipole trap depth, we therefore fit the images with a two-dimensional (2D) symmetric Gaussian up to 25 cm behind the axicon and with a 2D Bessel function at larger distances. For the Bessel fits we use

$$f(y,z) = A\mathcal{J}_0\left(\sqrt{(y-y_0)^2 + (z-z_0)^2}/s_B\right)^2, \qquad \text{(A1)}$$

where $\mathcal{J}_0$ is the zeroth-order Bessel function of the first kind and A, y_0, z_0 and s_B are free parameters. Sample crosscuts of the fitted and measured profiles are shown in Fig. 6.

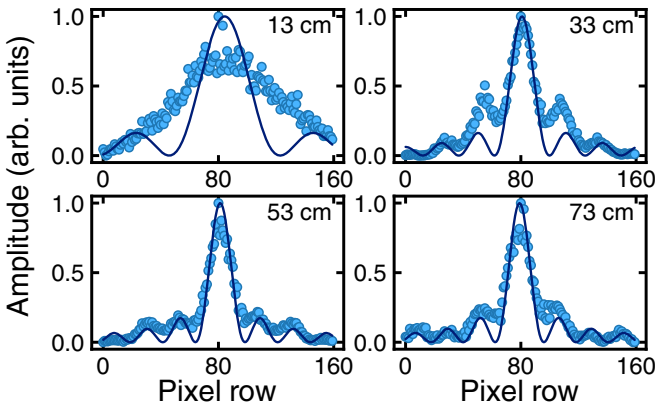

FIG. 6. Example fits of a Bessel function (blue line) to the measured Bessel beam profiles (blue points). The distance from the axicon is indicated in the top right.

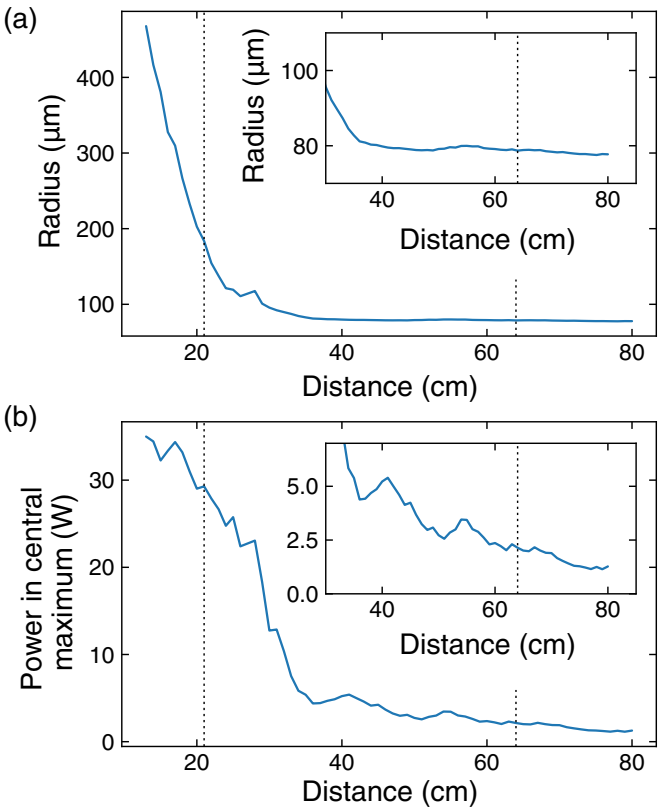

FIG. 7. (a) Fitted waists w_B of the Bessel-shaped transport beam versus distance from the axicon. The waists are computed from the fitted radii s_B. The inset shows a zoom of the region, which starts at 30 cm behind the axicon, indicating the diffractionless propagation of the Bessel beam. (b) Power in the central maximum, extracted from the peak intensity and the fitted radii shown in (a). The input power before the axicon is 35 W. The inset shows a zoom of the region starting 30 cm behind the axicon. The dashed vertical lines in both plots indicate the start and end positions of the transport.

From the Gaussian fits we can directly extract the waist of the beam for the computation of the depth of the dipole trap. For the Bessel fits, we map the fitted width to a Gaussian waist via $w_B = 1.3\sqrt{2}s_B$ [Fig. 7(a)]. We extract the relative peak intensity of the images versus distance by first subtracting a constant background from the images. Because the power was not kept constant for all measurements and instead was increased for long distances from the axicon, we evaluate the power-normalized peak intensity via the ratio $r(x) = I_{\max}/\sum_{\text{px}} I$, where $I_{\max}$ denotes the maximum pixel value and $\sum_{\text{px}} I$ corresponds to the pixel sum over the whole image, after subtracting a constant background. We then compute the relative peak intensity by normalizing $r(x)$ to the relative peak intensity after a distance of $x_{\text{ref}} = 13$ cm behind the axicon, $I_{\text{rel}} = r/r(x_{\text{ref}})$. In order to get an absolute value for the peak intensity $I_B = I_{\text{rel}} I_{\text{ref}}$ we multiply all values with the Gaussian peak intensity $I_{\text{ref}} = 2P/\pi w_{\text{ref}}^2$ at x_{ref}. Here the regular formula for a Gaussian beam is still applicable because the beam still has a Gaussian profile. The power contained in the central peak is shown in Fig. 7(b) for an incoming beam of 35 W as it was used in this work.

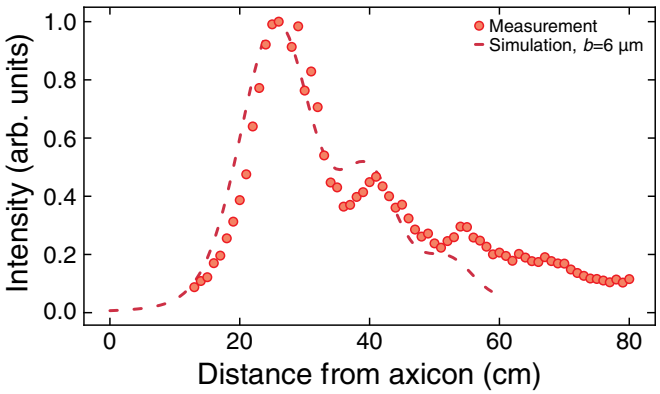

FIG. 8. Comparison of the measured Bessel intensity (red circles) with the theoretical intensity due to a round-tip axicon (dashed red line) with $b = 6\,\mu$m. Both the modulation and the low intensity at short distances are due to the round tip of the axicon.

An ideal axicon would result in a Gaussian intensity profile along the propagation direction. Imperfections can be modeled by assuming a round-tip axicon [57]. The effect of the round tip on the Bessel beam intensity is twofold: First, it reduces the peak power immediately behind the axicon, and second, it leads to a modulation of the intensity versus distance. Both effects are visible in our measurement. We find reasonable agreement between theory [Ref. [57], Eq. (6)] and experiment for a round-tip axicon with $b = 6\,\mu$m (Fig. 8). Here b is the semimajor axis of the hyperbola used in approximating the round tip of the axicon. The intensity of the Bessel beam remains low for the first few centimeters behind the axicon, and we observe secondary maxima after the initial intensity peak.

Lattice depth. We compute the lattice depth using the measured position of the waist of the Gaussian transport beam and its power P_G. The radius and the power in the central peak of the Bessel beam are shown in Fig. 7 for a total power of the incoming beam of 35 W. In Fig. 9 we show the calculated lattice depth for two different values of the powers of the Gaussian transport beam P_G, together with the vertical trap depth V_z. The lattice depth tends to be larger than the vertical potential depth for longer transport distances.

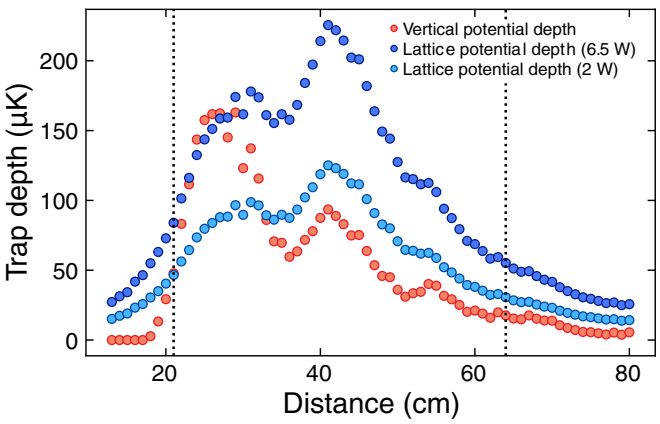

FIG. 9. Lattice depth for $P_G = 2$ W (light blue dots) and $P_G^{\mathrm{typ}} = 6.5$ W (dark blue dots). The vertical trap depth (red dots) was computed for P_G^{typ} [same data as in Fig. 2(b)]. The dashed lines indicate the start and end position of the transport.

2. Radio-frequency control of relative detuning

a. Frequency-shifting setup

For the transport lattice we use two ALS 45W Nd:YAG fiber amplifier systems. The two lasers are referred to as Gaussian and Bessel lasers according to which of the transport beams the laser generates. The Gaussian laser is seeded by a low RIN NPRO Mephisto S laser from Coherent. A small fraction of the light from the output of the Gaussian is split off and frequency shifted using two double-pass AOMs. One AOM shifts the frequency by $2f_1$ within the range $f_1 \in [150, 175]$ MHz; the other shifts the frequency by $2f_2$ within the range $f_2 \in [200, 225]$ MHz. The two AOMs shift the frequency in opposite directions. Because the Gaussian laser is intensity stabilized using a 100-MHz AOM, the static transport lattice is created with the two AOMs set to $2f_1 = 2 \times 175$ MHz and $2f_2 = 2 \times 225$ MHz. We transport the atoms towards the glass cell by tuning the frequencies to $f_2 = 200$ MHz and $f_1 = 175$ MHz and transport them back to the MOT chamber with $f_2 = 225$ MHz and $f_1 = 150$ MHz. The output of the double-DPAOM setup seeds the Bessel laser. This laser is not intensity stabilized beyond the internal stabilization circuitry.

The 225- and 175-MHz frequencies are generated by two AD9914 DDS evaluations boards. The frequency ramps use the internal linear ramp generator of the DDS boards with a typical frequency step of 550 Hz and a step rate of 0.2 μs. To change the acceleration, we change the frequency step size and keep the step rate fixed. We have also tested the transport using AD9910 DDS chips from a Wieser Lab FlexDDS-NG board and found no difference in transport efficiency. To decrease the radio-frequency (rf) linewidth we supply an external 2.5-GHz reference clock to the chips directly instead of relying on the chips' internal phase locked loop (PLL). This clock is locked to a 10-MHz Rb reference clock, which we also use as a clock for the frequency generator (R&S SMC100A) supplying 100 MHz for the Gaussian beam's intensity stabilization. This ensures reduced relative frequency drifts between the Gaussian and Bessel beams. Note that due to the 32-bit frequency resolution of the DDS chips, the default detuning of the Gaussian and Bessel beams is not zero but rather on the scale of a few millihertz.

b. Sensitivity to rf noise

To characterize the sensitivity of the transport to frequency noise we modulate the frequency of the 100-MHz intensity-stabilization AOM using Gaussian white noise. The white noise is generated from an arbitrary wave-form generator with a bandwidth of 10 MHz, a peak voltage of 1 V, and a crest factor of ∼4.3. The output of the wave-form generator is sent to the low-FM input of the signal generator for the AOM. We vary the amplitude of the frequency modulation by changing the modulation bandwidth of the signal generator. Figure 10(a) shows the atom number measured in the MOT chamber without transport but holding the atom in the lattice for 16 ms and the one in the glass cell after transport

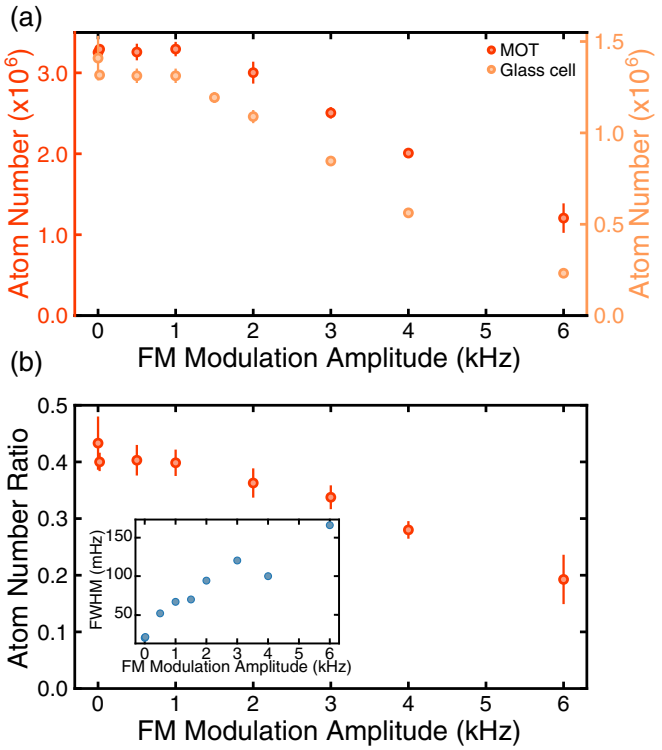

FIG. 10. (a) Atom number in the lattice versus frequency modulation bandwidth. The left axis shows the atoms remaining after holding them in the static lattice for 25.5 ms; the right axis shows the atoms arriving in the glass cell after transport. (b) Ratio of the atom numbers in the MOT and glass cell, indicating that the transport efficiency is reduced as the noise of the lattices is increased. The inset shows the FWHM linewidth of the rf source for the AOM shifting the frequency of the Gaussian beam as a function of FM amplitude.

($a_{\mathrm{typ}} = 2.9\,\mathrm{km/s^2}$, $P_G^{\mathrm{typ}} \lesssim 6.5\,\mathrm{W}$). We find that for modulation bandwidths > 1 kHz the atom number decreases in a similar fashion for both the atoms held in the lattice and the atoms transported. To estimate the change in transport efficiency due to the frequency modulation, we compute the ratio of the transported and held atom numbers and plot it in Fig. 10(b). We find that the modulation also affects the transport efficiency, reducing it linearly as the modulation amplitude is increased beyond 1 kHz. The inset in Fig. 10(b) shows the rf linewidth versus the modulation amplitude. The linewidth is extracted by fitting a Lorentzian to the signal generator's output spectrum measured with a spectrum analyzer. Since we can add small amounts of noise to the frequency of the Gaussian beam without worsening the transport efficiency, the transport efficiency is not limited by the frequency sources or relative drifts between them.

3. Transport efficiency measurements

a. Extended data

In Fig. 11 we show additional measurements of the transport efficiency that were taken for different values of P_G and a. In Figs. 3(c) and 3(d) we show crosscuts of this 2D plot.

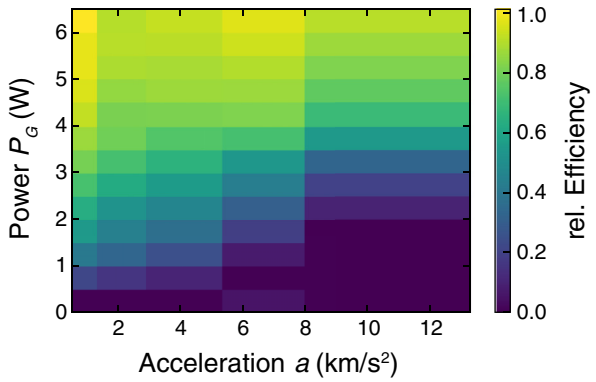

FIG. 11. One-way transport efficiency measurements. Figures 3(c) and 3(d) are crosscuts through this figure. The mean transport efficiency is normalized to the mean transport efficiency at $a = 0.5\,\mathrm{km/s^2}$ and $P_G = 6.5\,\mathrm{W}$. The mean is computed over five repetitions.

b. Normalization

The measurements in Figs. 3(c) and 3(d) are taken by measuring the atom number in the glass cell (one-way transport). To extract a relative efficiency, we use the mean atom number transported at the lowest acceleration of $a = 0.5\,\mathrm{km/s^2}$ and the highest power of the Gaussian transport beam $P_G^{\mathrm{typ}} = 6.5\,\mathrm{W}$ as a reference. The mean is calculated using five repeated measurements.

c. Guides to the eye in Figure 3

Before fitting the guides to the eye in Figs. 3(c) and 3(d), the data are filtered. For Figs. 3(c) and 3(d) all points with a relative efficiency $\eta > 0.75$ or $\eta < 0.1$ are ignored since we observe a saturation for low values of the acceleration and large powers, while there is essentially no transport for low values of the power P_G of the Gaussian transport beam. To account for the saturation in the acceleration data [Fig. 3(d)] we discard the points with accelerations smaller than

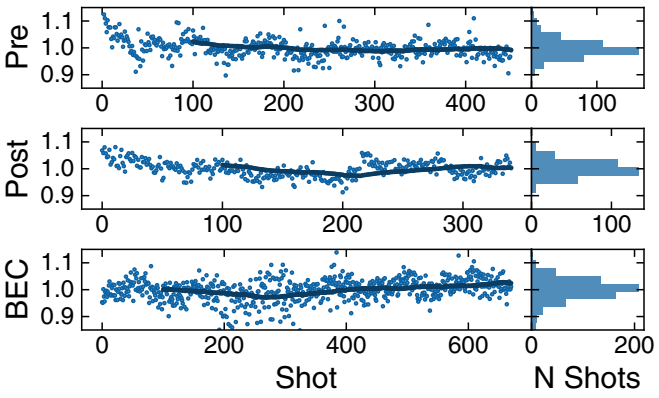

FIG. 12. Atom-number stability before (Pre) and immediately after (Post) transport and in the BEC [same data as in Fig. 4(d)]. As in Fig. 4(d), the dark blue points show mean values, which were obtained by averaging the individual data points in a time window of 20 min. The histograms on the right show the corresponding distributions.

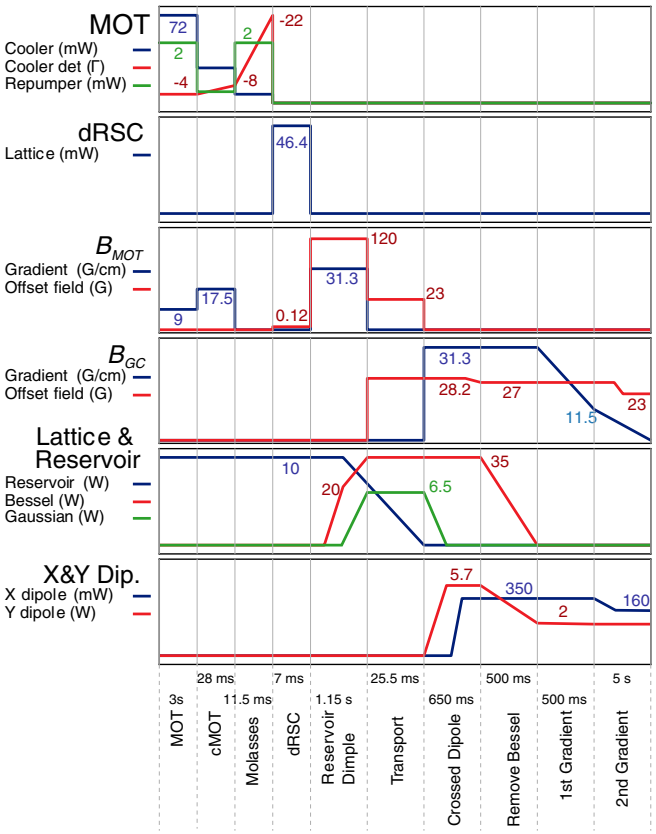

FIG. 13. Sketch of the sequence. The relative changes in detuning, power, and magnetic field B are shown for both the MOT chamber and the glass cell (GC). The horizontal and vertical axes are not to scale in order to improve readability.

$a = 5\,\mathrm{km/s^2}$ for the measurement with a power of $P_G^{\mathrm{typ}} = 6.5\,\mathrm{W}$.

We fit the data in Fig. 3(c) using $N(P) = b_1\sqrt{P_G} + b_0$, where b_1 and b_0 are free fit parameters, and the data in Fig. 3(d) using $N(a) = \tilde{b}_1 a + \tilde{b}_0$, with free parameters $\tilde{b}_1$ and $\tilde{b}_0$.

4. Atom-number stability before and after transport

In Fig. 12 we show how the transported atom number fluctuates between repeated measurements before and directly after the transport and compare the results to the fluctuations in final atom number in the BEC N_0. The histograms on the right show the distribution of the fluctuations for the corresponding measurements. For all data sets we have removed a slow drift, which is caused by the stabilization of the ambient temperature in the laboratory.

5. Experimental sequence

Laser cooling of ^{133}Cs atoms is performed on the D_2 line ($|6S_{1/2} \rightarrow P_{3/2}\rangle$, $\lambda_{D2} = 852$ nm). In the following we denote the $|F = 4\rangle \rightarrow |F' = 5\rangle$ transition as the cooling and $|F = 3\rangle \rightarrow |F' = 4\rangle$ as the repumping transition.

The experimental sequence starts by loading 3×10^7 atoms in a magneto-optical trap (MOT) from a Zeeman slower in 3 s. The cooling light of the MOT is -4Γ detuned from the cooling transition. Here $\Gamma = 2\pi \times 5.2\,\mathrm{MHz}$ [67] represents the linewidth of the D_2 line. Additionally, 2 mW of resonant light in the repumper transition are required to prevent depumping. After MOT loading, we perform a compressed MOT stage to increase the density of the cloud. In 28 ms we increase the magnetic field gradient from 9 to 17.5 G/cm and the cooler detuning to -8Γ. Simultaneously, we reduce the cooler and repumper power to 25 mW and 60 μW, respectively. We subsequently switch off the gradient and increase the cooler detuning to -22Γ for an 11.5-ms-long molasses phase. In order to improve the cooling efficiency during this stage the residual magnetic fields are compensated with an accuracy of 50 mG. Typically, we obtain at the end of the molasses phase 3×10^7 atoms, comparable to the MOT phase, with a temperature of 10 μK.

After molasses, the atoms are optically pumped into $|F = 3\rangle$, where degenerate Raman sideband cooling (dRSC) is performed in a three-dimensional optical lattice. The Raman lattice is -20 GHz detuned from $|F = 3\rangle \rightarrow |F' = 2\rangle$ resonance. The lattice is generated by interfering three orthogonal beams along the $\tilde{x}$, $\tilde{y}$, and z directions. Here the $(\tilde{x}, \tilde{y})$ axis denotes a rotation of 30° with respect to the coordinate system shown in Fig. 1(a). The $\tilde{y}$-lattice beam is retroreflected after passing through a $\lambda/4$ wave plate. The beams are linearly polarized. The $\tilde{x}$ and z beams are polarized such that they interfere only with the $\tilde{y}$ beam. In addition to the lattice, a circularly polarized beam propagates along the z direction. This beam is resonant with the $|F = 3\rangle \rightarrow |F' = 2\rangle$ transition with a power of 650 μW. After 7 ms of dRSC cooling we obtain 2×10^7 atoms at <1 μK at a density of 3×10^{10} atoms/cm^3. The following steps towards condensation are described in the main text.

A detailed sequence for producing degenerate gases of cesium atoms is presented in Fig. 13. This includes the relative changes in detuning, power, and magnetic fields either in the glass cell or in the MOT chamber. We sketch the respective values for the start and end of the ramps.

[1] I. M. Georgescu, S. Ashhab, and F. Nori, Quantum simulation, Rev. Mod. Phys. **86**, 153 (2014).

[2] C. Gross and I. Bloch, Quantum simulations with ultracold atoms in optical lattices, Science **357**, 995 (2017).

[3] F. Schäfer, T. Fukuhara, S. Sugawa, Y. Takasu, and Y. Takahashi, Tools for quantum simulation with ultracold atoms in optical lattices, Nat. Rev. Phys. **2**, 411 (2020).

[4] A. Browaeys and T. Lahaye, Many-body physics with individually controlled Rydberg atoms, Nat. Phys. **16**, 132 (2020).

[5] C. Schweizer, F. Grusdt, M. Berngruber, L. Barbiero, E. Demler, N. Goldman, I. Bloch, and M. Aidelsburger, Floquet approach to $\mathbb{Z}_2$ lattice gauge theories with ultracold atoms in optical lattices, Nat. Phys. **15**, 1168 (2019).

[6] F. M. Surace, P. P. Mazza, G. Giudici, A. Lerose, A. Gambassi, and M. Dalmonte, Lattice Gauge Theories and String

Dynamics in Rydberg Atom Quantum Simulators, Phys. Rev. X **10**, 021041 (2020).

[7] A. Mil, T. V. Zache, A. Hegde, A. Xia, R. P. Bhatt, M. K. Oberthaler, P. Hauke, J. Berges, and F. Jendrzejewski, A scalable realization of local U(1) gauge invariance in cold atomic mixtures, Science **367**, 1128 (2020).

[8] B. Yang, H. Sun, R. Ott, H.-Y. Wang, T. V. Zache, J. C. Halimeh, Z.-S. Yuan, P. Hauke, and J.-W. Pan, Observation of gauge invariance in a 71-site Bose–Hubbard quantum simulator, Nature (London) **587**, 392 (2020).

[9] A. Periwal, E. S. Cooper, P. Kunkel, J. F. Wienand, E. J. Davis, and M. Schleier-Smith, Programmable interactions and emergent geometry in an atomic array, Nature **600**, 630 (2021).

[10] G. Bentsen, T. Hashizume, A. S. Buyskikh, E. J. Davis, A. J. Daley, S. S. Gubser, and M. Schleier-Smith, Treelike Interactions and Fast Scrambling with Cold Atoms, Phys. Rev. Lett. **123**, 130601 (2019).

[11] R. Belyansky, P. Bienias, Y. A. Kharkov, A. V. Gorshkov, and B. Swingle, Minimal Model for Fast Scrambling, Phys. Rev. Lett. **125**, 130601 (2020).

[12] A. R. Brown, H. Gharibyan, S. Leichenauer, H. W. Lin, S. Nezami, G. Salton, L. Susskind, B. Swingle, and M. Walter, Quantum gravity in the lab: teleportation by size and traversable wormholes, arXiv:1911.06314.

[13] M. C. Bañuls *et al.*, Simulating lattice gauge theories within quantum technologies, Eur. Phys. J. D **74**, 165 (2020).

[14] M. Aidelsburger *et al.*, Cold atoms meet lattice gauge theory, Phil. Trans. R. Soc. A. **380**, 20210064 (2021).

[15] S. Trotzky, Y.-A. Chen, A. Flesch, I. P. McCulloch, U. Schollwöck, J. Eisert, and I. Bloch, Probing the relaxation towards equilibrium in an isolated strongly correlated one-dimensional Bose gas, Nat. Phys. **8**, 325 (2012).

[16] S. Ebadi, T. T. Wang, H. Levine, A. Keesling, G. Semeghini, A. Omran, D. Bluvstein, R. Samajdar, H. Pichler, W. W. Ho, S. Choi, S. Sachdev, M. Greiner, V. Vuletic, and M. D. Lukin, Quantum phases of matter on a 256-atom programmable quantum simulator, Nature (London) **595**, 227 (2021).

[17] P. Scholl, M. Schuler, H. J. Williams, A. A. Eberharter, D. Barredo, K.-N. Schymik, V. Lienhard, L.-P. Henry, T. C. Lang, T. Lahaye, A. M. Läuchli, and A. Browaeys, Quantum simulation of 2D antiferromagnets with hundreds of Rydberg atoms, Nature (London) **595**, 233 (2021).

[18] B. Hebbe Madhusudhana, S. Scherg, T. Kohlert, I. Bloch, and M. Aidelsburger, Benchmarking a novel efficient numerical method for localized 1d fermi-hubbard systems on a quantum simulator, PRX Quantum **2**, 040325 (2021).

[19] A. D. Ludlow, M. M. Boyd, J. Ye, E. Peik, and P. O. Schmidt, Optical atomic clocks, Rev. Mod. Phys. **87**, 637 (2015).

[20] L. Henriet, L. Beguin, A. Signoles, T. Lahaye, A. Browaeys, G.-O. Reymond, and C. Jurczak, Quantum computing with neutral atoms, Quantum **4**, 327 (2020).

[21] C. Gross and W. S. Bakr, Quantum gas microscopy for single atom and spin detection, Nature Phys. **17**, 1316 (2021).

[22] T. Kinoshita, T. Wenger, and D. S. Weiss, All-optical Bose-Einstein condensation using a compressible crossed dipole trap, Phys. Rev. A **71**, 011602(R) (2005).

[23] S. Stellmer, B. Pasquiou, R. Grimm, and F. Schreck, Laser Cooling to Quantum Degeneracy, Phys. Rev. Lett. **110**, 263003 (2013).

[24] S. Stellmer, R. Grimm, and F. Schreck, Production of quantum-degenerate strontium gases, Phys. Rev. A **87**, 013611 (2013).

[25] R. Roy, A. Green, R. Bowler, and S. Gupta, Rapid cooling to quantum degeneracy in dynamically shaped atom traps, Phys. Rev. A **93**, 043403 (2016).

[26] J. Hu, A. Urvoy, Z. Vendeiro, V. Crépel, W. Chen, and V. Vuletić, Creation of a Bose-condensed gas of ^{87} Rb by laser cooling, Science **358**, 1078 (2017).

[27] A. Urvoy, Z. Vendeiro, J. Ramette, A. Adiyatullin, and V. Vuletić, Direct Laser Cooling to Bose-Einstein Condensation in a Dipole Trap, Phys. Rev. Lett. **122**, 203202 (2019).

[28] P. Solano, Y. Duan, Y.-T. Chen, A. Rudelis, C. Chin, and V. Vuletić, Strongly Correlated Quantum Gas Prepared by Direct Laser Cooling, Phys. Rev. Lett. **123**, 173401 (2019).

[29] G. A. Phelps, A. Hébert, A. Krahn, S. Dickerson, F. Ötürk, S. Ebadi, L. Su, and M. Greiner, Sub-second production of a quantum degenerate gas, arXiv:2007.10807.

[30] A. Z. Lam, C. Warner, N. Bigagli, S. Roschinski, W. Yuan, I. Stevenson, and S. Will, Compact two-dimensional magneto-optical trap for ultracold atom setups, arXiv:2012.06688.

[31] P. Kómár, E. M. Kessler, M. Bishof, L. Jiang, A. S. Sørensen, J. Ye, and M. D. Lukin, A quantum network of clocks, Nat. Phys. **10**, 582 (2014).

[32] S. Koller, J. Grotti, S. Vogt, A. Al-Masoudi, S. Dörscher, S. Häfner, U. Sterr, and C. Lisdat, Transportable Optical Lattice Clock with 7×10^{-17} Uncertainty, Phys. Rev. Lett. **118**, 073601 (2017).

[33] K. Bongs, M. Holynski, J. Vovrosh, P. Bouyer, G. Condon, E. Rasel, C. Schubert, W. P. Schleich, and A. Roura, Taking atom interferometric quantum sensors from the laboratory to real-world applications, Nat. Rev. Phys. **1**, 731 (2019).

[34] E. Altman *et al.*, Quantum simulators: architectures and opportunities, PRX Quantum, **2**, 017003 (2021).

[35] M. Greiner, I. Bloch, T. W. Hänsch, and T. Esslinger, Magnetic transport of trapped cold atoms over a large distance, Phys. Rev. A **63**, 031401(R) (2001).

[36] H. J. Lewandowski, D. M. Harber, D. L. Whitaker, and E. A. Cornell, Observation of Anomalous Spin-State Segregation in a Trapped Ultracold Vapor, Phys. Rev. Lett. **88**, 070403 (2002).

[37] D. Pertot, D. Greif, S. Albert, B. Gadway, and D. Schneble, Versatile transporter apparatus for experiments with optically trapped Bose–Einstein condensates, J. Phys. B **42**, 215305 (2009).

[38] D. Schrader, S. Kuhr, W. Alt, M. Müller, V. Gomer, and D. Meschede, An optical conveyor belt for single neutral atoms, Appl. Phys. B **73**, 819 (2001).

[39] S. Schmid, G. Thalhammer, K. Winkler, F. Lang, and J. H. Denschlag, Long distance transport of ultracold atoms using a 1D optical lattice, New J. Phys. **8**, 159 (2006).

[40] A. L. Marchant, S. Händel, T. P. Wiles, S. A. Hopkins, and S. L. Cornish, Guided transport of ultracold gases of rubidium up to a room-temperature dielectric surface, New J. Phys. **13**, 125003 (2011).

[41] T. Middelmann, S. Falke, C. Lisdat, and U. Sterr, Long-range transport of ultracold atoms in a far-detuned one-dimensional optical lattice, New J. Phys. **14**, 073020 (2012).

[42] J. Léonard, M. Lee, A. Morales, T. M. Karg, T. Esslinger, and T. Donner, Optical transport and manipulation of an ultracold atomic cloud using focus-tunable lenses, New J. Phys. **16**, 093028 (2014).

[43] C. Gross, H. C. J. Gan, and K. Dieckmann, All-optical production and transport of a large ^{6}Li quantum gas in a crossed optical dipole trap, Phys. Rev. A **93**, 053424 (2016).

[44] M. Langbecker, R. Wirtz, F. Knoch, M. Noaman, T. Speck, and P. Windpassinger, Highly controlled optical transport of cold atoms into a hollow-core fiber, New J. Phys. **20**, 083038 (2018).

[45] G. Unnikrishnan, C. Beulenkamp, D. Zhang, K. P. Zamarski, M. Landini, and H.-C. Nägerl, Long distance optical transport of ultracold atoms: A compact setup using a moiré lens, Rev. Sci. Instrum. **92**, 063205 (2021).

[46] J. H. Lee, H. Jung, J.-y. Choi, and J. Mun, Transporting cold atoms using an optically compensated zoom lens, Phys. Rev. A **102**, 063106 (2020).

[47] A. Couvert, T. Kawalec, G. Reinaudi, and D. Guéry-Odelin, Optimal transport of ultracold atoms in the non-adiabatic regime, Europhys. Lett. **83**, 13001 (2008).

[48] W. S. Bakr, J. I. Gillen, A. Peng, S. Fölling, and M. Greiner, A quantum gas microscope for detecting single atoms in a Hubbard-regime optical lattice, Nature (London) **462**, 74 (2009).

[49] J. F. Sherson, C. Weitenberg, M. Endres, M. Cheneau, I. Bloch, and S. Kuhr, Single-atom-resolved fluorescence imaging of an atomic Mott insulator, Nature (London) **467**, 68 (2010).

[50] R. Yamamoto, J. Kobayashi, T. Kuno, K. Kato, and Y. Takahashi, An ytterbium quantum gas microscope with narrow-line laser cooling, New J. Phys. **18**, 023016 (2016).

[51] L. W. Cheuk, M. A. Nichols, M. Okan, T. Gersdorf, V. V. Ramasesh, W. S. Bakr, T. Lompe, and M. W. Zwierlein, Quantum-Gas Microscope for Fermionic Atoms, Phys. Rev. Lett. **114**, 193001 (2015).

[52] E. Haller, J. Hudson, A. Kelly, D. A. Cotta, B. Peaudecerf, G. D. Bruce, and S. Kuhr, Single-atom imaging of fermions in a quantum-gas microscope, Nat. Phys. **11**, 738 (2015).

[53] G. J. A. Edge, R. Anderson, D. Jervis, D. C. McKay, R. Day, S. Trotzky, and J. H. Thywissen, Imaging and addressing of individual fermionic atoms in an optical lattice, Phys. Rev. A **92**, 063406 (2015).

[54] M. F. Parsons, F. Huber, A. Mazurenko, C. S. Chiu, W. Setiawan, K. Wooley-Brown, S. Blatt, and M. Greiner, Site-Resolved Imaging of Fermionic ^{6}Li in an Optical Lattice, Phys. Rev. Lett. **114**, 213002 (2015).

[55] A. Omran, M. Boll, T. A. Hilker, K. Kleinlein, G. Salomon, I. Bloch, and C. Gross, Microscopic Observation of Pauli Blocking in Degenerate Fermionic Lattice Gases, Phys. Rev. Lett. **115**, 263001 (2015).

[56] A. Alberti, C. Robens, W. Alt, S. Brakhane, M. Karski, R. Reimann, A. Widera, and D. Meschede, Super-resolution microscopy of single atoms in optical lattices, New J. Phys. **18**, 053010 (2016).

[57] O. Brzobohatý, T. Čižmár, and P. Zemánek, High quality quasi-Bessel beam generated by round-tip axicon, Opt. Express **16**, 12688 (2008).

[58] T. Weber, J. Herbig, M. Mark, H.-C. Nägerl, and R. Grimm, Bose-Einstein condensation of cesium, Science **299**, 232 (2003).

[59] A. J. Kerman, V. Vuletić, C. Chin, and S. Chu, Beyond Optical Molasses: 3D Raman Sideband Cooling of Atomic Cesium to High Phase-Space Density, Phys. Rev. Lett. **84**, 439 (2000).

[60] C. Chin, V. Vuletić, A. J. Kerman, S. Chu, E. Tiesinga, P. J. Leo, and C. J. Williams, Precision Feshbach spectroscopy of ultracold Cs_2, Phys. Rev. A **70**, 032701 (2004).

[61] P. Carruthers and M. M. Nieto, Coherent states and the forced quantum oscillator, Am. J. Phys. **33**, 537 (1965).

[62] E. Torrontegui, S. Ibáñez, X. Chen, A. Ruschhaupt, D. Guéry-Odelin, and J. G. Muga, Fast atomic transport without vibrational heating, Phys. Rev. A **83**, 013415 (2011).

[63] C.-L. Hung, X. Zhang, N. Gemelke, and C. Chin, Accelerating evaporative cooling of atoms into Bose-Einstein condensation in optical traps, Phys. Rev. A **78**, 011604(R) (2008).

[64] T. Kraemer, M. Mark, P. Waldburger, J. G. Danzl, C. Chin, B. Engeser, A. D. Lange, K. Pilch, A. Jaakkola, H.-C. Nägerl, and R. Grimm, Evidence for Efimov quantum states in an ultracold gas of caesium atoms, Nature (London) **440**, 315 (2006).

[65] M. Gröbner, P. Weinmann, F. Meinert, K. Lauber, E. Kirilov, and H.-C. Nägerl, A new quantum gas apparatus for ultracold mixtures of K and Cs and KCs ground-state molecules, J. Mod. Opt. **63**, 1829 (2016).

[66] I. H. Malitson, Interspecimen comparison of the refractive index of fused silica, J. Opt. Soc. Am. **55**, 1205 (1965).

[67] D. A. Steck, Cesium D line data, revision 2.2.1 (2019).